JGR Solid Earth

RESEARCH ARTICLE
10.1029/2021JB021897

Key Points:

- Waveform modeling of SKKS, SKS, and SPdKS amplitudes and travel-times put greater constraints on ultralow-velocity zone (ULVZ) size and elastic parameters
- Data are fit with a 1.3 δV_S to δV_P ratio which may be indicative of a compositional origin
- The long linear shape of the Samoa ULVZ may indicates this ULVZ is currently moving across the core-mantle boundary

Supporting Information:

Supporting Information may be found in the online version of this article.

Correspondence to:

M. S. Thorne,
michael.thorne@utah.edu

Citation:

Krier, J., Thorne, M. S., Leng, K., & Nissen-Meyer, T. (2021). A compositional component to the Samoa ultralow-velocity zone revealed through 2- and 3-D waveform modeling of SKS and SKKS differential travel-times and amplitudes. *Journal of Geophysical Research: Solid Earth*, *126*, e2021JB021897. https://doi.org/10.1029/2021JB021897

Received 19 FEB 2021
Accepted 14 JUN 2021

A Compositional Component to the Samoa Ultralow-Velocity Zone Revealed Through 2- and 3-D Waveform Modeling of SKS and SKKS Differential Travel-Times and Amplitudes

Justin Krier[1], Michael S. Thorne[1], Kuangdai Leng[2], and Tarje Nissen-Meyer[2]

[1]University of Utah, Salt Lake City, UT, USA, [2]Department of Earth Sciences, University of Oxford, Oxford, UK

Abstract We analyzed 4,754 broadband seismic recordings of the SKS, SKKS, and SPdKS wavefield from 13 high quality events sampling the Samoa ultralow-velocity zone (ULVZ). We measured differential travel-times and amplitudes between the SKKS and SKS arrivals, which are highly sensitive to the emergence of the SPdKS seismic phase, which is in turn highly sensitive to lowermost mantle velocity perturbations such as generated by ULVZs. We modeled these data using a 2-D axi-symmetric waveform modeling approach and are able to explain these data with a single ULVZ. In order to predict both travel-time and amplitude perturbations we found that a large ULVZ length in the great circle arc direction on the order of 10° or larger is required. The large ULVZ length limits acceptable ULVZ elastic parameters. Here we find that δV_S and δV_P reductions from 20% to 22% and 15% to 17% respectively gives us the best fit, with a thickness of 26 km. Initial 3-D modeling efforts do not recover the extremes in the differential measurements, demonstrating that 3-D effects are important and must be considered in the future. However, the 3-D modeling is generally consistent with the velocity reductions recovered with the 2-D modeling. These velocity reductions are compatible with a compositional component to the ULVZ. Furthermore, geodynamic predictions for a compositional ULVZ that is moving predict a long linear shape similar to the shape of the Samoa ULVZ we confirm in this study.

Plain Language Summary Ultralow-velocity zones (ULVZs) on the core-mantle boundary (CMB) are some of the most extreme features discovered in Earth's mantle. What ULVZs physically represent and how they have arisen in the Earth are still open questions. Important clues about the origin and makeup of ULVZs may come from studying the Samoa ULVZ which, with a length of approximately 1,600 km along the CMB, is the largest ULVZ yet discovered. We used a new collection of seismic data with greater sensitivity to the Samoa ULVZ than has been used in previous studies to determine its physical properties. We determine ULVZ properties by comparing computations of what seismic waveforms look like for various ULVZ models to the data we collected. Our analysis suggests that the Samoa ULVZ is likely a compositional anomaly. Recent geodynamic modeling suggests that a compositional anomaly that is being advected along the CMB will take on a long linear shape similar to the shape we observe for the Samoa ULVZ. If some of the Samoa ULVZ material is being entrained into recent hot spot volcanism in the Samoa hot spot chain, then geochemical evidence from the volcanism may imply that the ULVZ is derived from ancient subducted slab material.

1. Introduction

Thin regions sitting on top of the core-mantle boundary (CMB) with *P*- and *S*-wave velocity reductions as large as 25%–45% respectively, known as ultralow-velocity zones (ULVZs) have been investigated using seismic techniques for nearly three decades. Evidence continues to accumulate that some of the ULVZs discovered may be linked to deep seated roots of whole mantle plumes that give rise to hot spot volcanism. Seismic waveform modeling has inferred large-scale ULVZs beneath hot spots such as Hawaii (Cottaar & Romanowicz, 2012), Samoa (Thorne, Garnero, et al., 2013), and Iceland (Helmberger et al., 1998; Yuan & Romanowicz, 2017). Additional evidence has been presented suggesting that ULVZs may also exist beneath hot spots such as Comores (Wen, 2000), Yellowstone (Nelson & Grand, 2018), Galapagos (Cottaar & Li, 2019), Marquesas (Kim et al., 2020), Caroline, and San Felix (Thorne et al., 2020). Furthermore, seismic

Table 1
Previous ULVZ Studies Beneath Samoa

#	Reference	Seismic phases	δV_S (%)[a]	δV_P (%)[a]	Thickness (km)	Dimensions on CMB (km)
1	Garnero et al. (1993)	LP SPdKS	-	5	100	-
2	Garnero and Helmberger (1995)	LP SKS, SKKS, SPdKS	10 or 5	10 or 5	20 or 100	-
3	Garnero and Helmberger (1996)	LP SKS, SKKS, SPdKS	-	10	40	-
4	Wen and Helmberger (1998a)	BB SPdKS	30	10	40	250 to 400 laterally
5	Y. Zhang et al. (2009)	BB SKS, SKKS	20–30	-	10–20	-
6	Thorne, Zhang, and Ritsema (2013)	BB SKS, SKKS	30	-	20	-
7	Thorne, Garnero, et al. (2013)	BB SPdKS	45	15	10–15	250 × 800
8	Thorne et al. (2021)	BB SPdKS	-	-	-	480 × 1,600

Abbreviations: BB, broadband; CMB, core-mantle boundary; LP, long period; ULVZ, ultralow-velocity zone.
[a]Percent reduction with respect to PREM.

tomography has begun to image whole mantle plumes, possibly rooted in ULVZs at the CMB coupled to hot spots at the surface (French & Romanowicz, 2015; Montelli et al., 2006). ULVZs were initially linked directly to hot spot genesis (Williams et al., 1998) and a partially molten origin which was supported by consistency of observations with 3:1 *S*- to *P*-wave velocity ratios (Williams & Garnero, 1996) but may also be tied to the boundaries of or within large low velocity provinces (LLVPs) (Garnero et al., 2016). However, not all large ULVZs are necessarily related to hot spot volcanism (Thorne et al., 2019, 2020), and although a partially molten origin to ULVZs is intriguing, some ULVZs may have a compositional origin as seismic observations are often also supported by a 1:1 or 2:1 *S*- to *P*-wave velocity ratio (Brown et al., 2015; Li et al., 2017; Wicks et al., 2010).

Anomalous structure beneath the Samoa hot spot was presented in the earliest ULVZ studies (Garnero & Helmberger, 1995, 1996; Garnero et al., 1993; Wen & Helmberger, 1998a), although these studies did not specifically link ULVZs to hot spots (see Table 1 for a review of ULVZ parameters reported). These efforts, using the seismic phase SPdKS (an SKS wave with an additional leg of *P*-diffraction along the CMB, see Figure 1) estimated ULVZ properties over a wide range of values including: (a) *S*-wave velocity (δV_S) decreases from 5% to 30% with respect to PREM (Dziewonski & Anderson, 1981), (b) *P*-wave velocity decreases (δV_P) from 5% to 10%, (c) thickness from 20 to 100 km, and (d) lateral dimensions of 250–400 km on the CMB. Among these studies, Garnero and Helmberger (1996) was the first to demonstrate that SKKS travel-time anomalies are also consistent with ULVZ presence in the region, although even older studies had already recognized that SKKS and SKS travel-times and amplitudes in this region would require modification of existing 1-D Earth models to explain (Kind & Müller, 1977; Schweitzer & Müller, 1986). The initial studies used the long period data and initially postulated a thick (on the order of 100 km) low velocity layer with *P*-wave velocity perturbations on the order of 5%. But subsequent studies using the broadband data recognized that an unobserved SKS precursor should be apparent for such a thick ULVZ and opted for thinner ULVZ models. Y. Zhang et al. (2009) considered SKKS/SKS amplitude ratios and showed that a 10–20 km thick ULVZ with δV_S reductions of 20%–30% was consistent with the anomalously high amplitude ratios. However, this study neglected to locate the ULVZ. Thorne, Zhang, and Ritsema (2013) also considered SKKS-SKS differential travel-times for a ULVZ embedded in the seismic tomography model S40RTS (Ritsema et al., 2010); again, demonstrating the need for a 20 km thick ULVZ in the region. Localization of the ULVZ beneath Samoa was first presented in Thorne, Garnero, et al. (2013). This study argued for a ULVZ at least 250 × 800 km across, making the Samoa ULVZ one of the largest-scale yet detected. More recently, Thorne et al. (2020, 2021) analyzed a global collection of highly anomalous SPdKS waveforms showing that the Samoa ULVZ may span an area as large as 480 × 1,600 km. The scale and linear morphology of the Samoa ULVZ is unique. ULVZs beneath Iceland (Yuan & Romanowicz, 2017) or Hawaii (Cottaar & Romanowicz, 2012; Kim et al., 2020) may rival the Samoa ULVZ in size, but at least initially appeared to be rounded features, rather than the long linear feature observed beneath Samoa. However, we note that recent studies suggest that ULVZ structure beneath Hawaii may also be significantly larger and more complicated than originally imaged (Jenkins et al., 2021; Zhao et al., 2016).

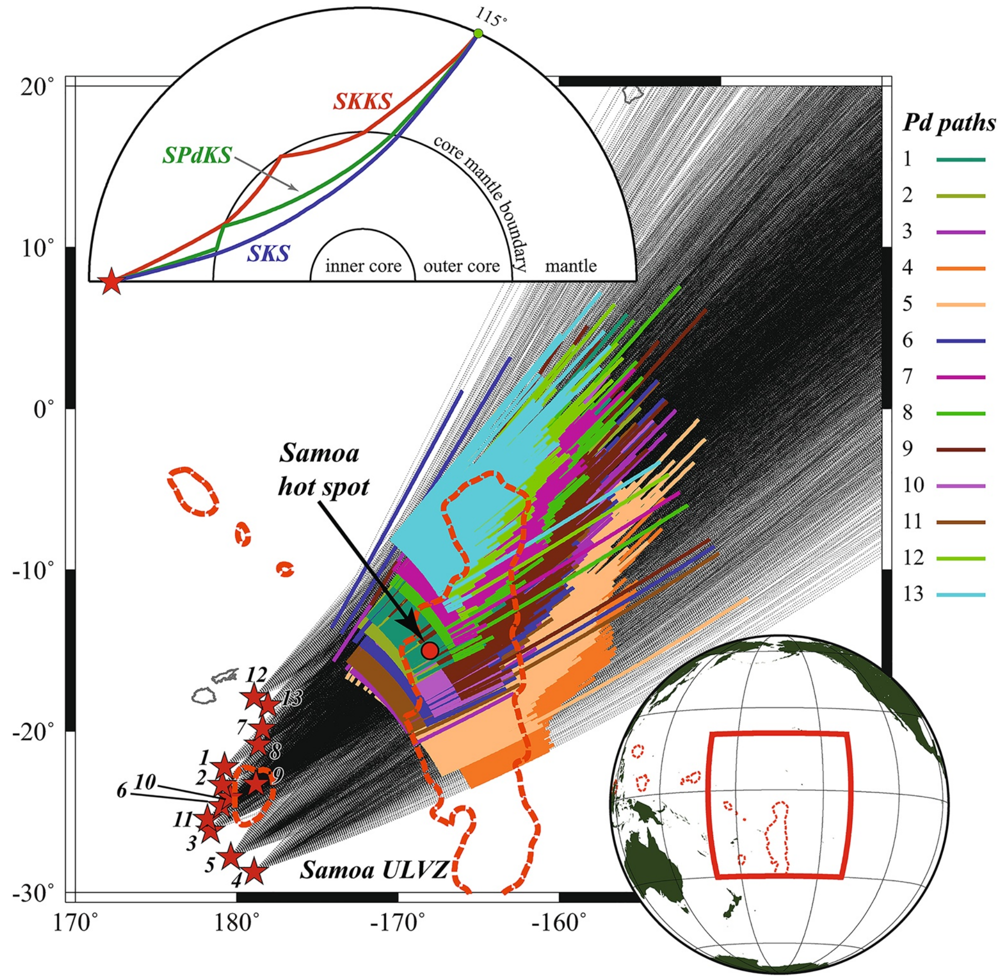

Figure 1. Upper left: Ray paths of seismic phases used in this study. Ray paths are drawn for receiver (green dot) located 115° from the earthquake (red star). Shown are SKS (blue), SPdKS (green), and SKKS (red). Main plot: Location of 13 earthquakes (red stars) analyzed. The numbers to the left of the stars correspond to the earthquake numbers in Table 2. Great circle arc paths are drawn as dashed black lines. Pd segments of SPdKS on the core-mantle boundary are thick lines shaded by event. The shading is shown in the legend to the right of the plot by event number. The dashed green lines show the position of the ultralow-velocity zone (ULVZ) modeled. The dashed orange lines provide the ULVZ contour at the probability = 0.5 level from Thorne et al. (2020). The red dot at the center of the ULVZ shows the location of the Samoa hot spot. The inset in the lower right-hand corner shows the location of the study region with the 0.5 ULVZ probability contours from Thorne et al. (2020) drawn with the dashed orange lines.

The Samoa hot spot shows one of the clearest whole mantle plume signatures in seismic tomography (French & Romanowicz, 2015; Montelli et al., 2006). However, volcanism along the Samoa line shows a wide array of isotopic taxonomies spanning the major Ocean Island Basalt end members. Although a high degree of heterogeneity exists in the older volcanism, the most recent volcanism has a weak himu (high μ, or high $^{238}U/^{204}Pb$ ratio) signature, which has been argued to descend from ancient subducted oceanic crust (Jackson et al., 2014). However, Samoa has the largest EM2 (enriched mantle) signature of all hot spots (Jackson et al., 2007) which is linked to ancient subducted continental crust. Furthermore, Samoa has the second highest $^{3}He/^{4}He$ ratio among the hot spots in the Pacific (Jackson et al., 2021) which is linked to high buoyancy flux and a deep-seated origin as a signature of primordial material. Thus, these lines of evidence point to a deep origin to the Samoa hot spot, although it is unknown if ULVZ material can be entrained into upwelling plumes and contribute to the isotopic diversity several studies have suggested this possibility (e.g., Jones et al., 2019; J. Zhang et al., 2018).

Table 2
Events Used in This Study

#	Mo/Day/Year	H:M:S	Lat (°)	Lon (°)	Depth (km)	Mag	Azimuth (°)	NR[a]
1	6/30/02	21:29:36	−22.010	179.250	620	6.5	40–70	73
2	6/30/10	4:31:02	−23.307	179.116	581	6.4	40–70	143
3	2/21/11	10:57:52	−26.142	178.494	558	6.5	30–70	395
4	4/26/13	6:53:29	−28.681	−178.916	351	6.1	40–70	479
5	8/28/13	2:54:41	−27.783	179.634	478	6.2	30–70	692
6	5/4/14	9:15:53	−24.611	179.086	527	6.6	30–70	678
7	7/21/14	14:54:41	−19.801	−178.400	614	6.9	40–70	520
8	5/27/16	4:08:44	−20.810	−178.648	567	6.4	40–70	304
9	2/24/17	17:28:45	−21.259	−178.804	414	6.9	30–70	339
10	6/17/17	22:26:02	−24.093	179.604	511	6.1	40–70	200
11	9/16/18	21:11:48	−25.415	178.199	576	6.5	40–70	348
12	9/30/18	10:52:23	−18.360	−178.063	550	6.7	40–70	298
13	11/18/18	20:25:46	−17.873	−178.927	540	6.8	40–70	285

[a]NR is the number of records used for epicentral distances from 100° to 130° for the azimuth range indicated.

In this study, we further examine the Samoa ULVZ by modeling the SKS, SPdKS, and SKKS wavefield (Figure 1) based on measurements of differential travel-times and amplitudes between SKKS and SKS, which are intimately linked to the generation of SPdKS. We show that only a limited range of ULVZ models can explain these data. In particular, we show that the lateral width of the Samoa ULVZ may be as large as 700 km with a thickness of 26 km. The inferred ULVZ elastic parameters and linear morphology of the Samoa ULVZ is consistent with a compositional origin that could in part be derived from ancient subduction.

2. Seismic Data

Seismic data used in this study were initially drawn from the data set collected in Thorne et al. (2020). In that study, a global set of the broadband seismic data were collected from 1990 to 2017. A total of 271,602 high quality radial component seismograms in the epicentral distance range from 90° to 130° for 1,146 events with depths ≥75 km were retained. The data from this previous study were subsequently augmented by adding 26 events and 10,972 additional records from 2018. Thorne et al. (2020) provide details on the data processing and selection process, but in summary, the primary data processing steps were: (a) the mean and trend of the traces were removed, (b) traces with gaps within the SKS/SKKS time window were removed, (c) instrument response was removed, (d) traces were integrated to displacement, and (e) rotated to the radial component. Similar to Thorne et al. (2020), we apply a two pass Butterworth filter to these data in the period band from 6 to 40 s before further analysis.

For this study, we selected 13 high quality events that sample the Samoa ULVZ as inferred from previous studies (Thorne et al., 2020; Thorne, Garnero, et al., 2013). These events were chosen based on the following criteria. First, only events with depths greater than 300 km were considered. This is in order to remove constructive/destructive interference from depth phases such as sSKS and pSKS. Second, we selected the events with the greatest density of recordings passing through the Samoa ULVZ and the highest signal-to-noise ratio. Details on the events selected are shown in Table 2 and their locations are shown in Figure 1. Also shown in Figure 1 is the location of the Pd segments of SPdKS along the CMB for these events.

In this study, we only consider records in the distance range from 100° to 130° because SKKS is not well developed at the shorter distances. We also only consider recordings that cross the Samoa ULVZ, in the azimuthal range from 30° or 40° to 70° (depending on event, see Table 2). Thus, we use a total of 4,754 seismograms in this study recorded in North America.

3. Methods

3.1. Differential Travel-Time and Amplitude Measurements

Similar to previous studies (Thorne, Zhang, & Ritsema, 2013; Y. Zhang et al., 2009), we measure differential travel-times and amplitudes between SKKS and SKS relative to a reference model. We define the travel-time difference as

$$\delta T_{\mathrm{SKKS}} = T^{\mathrm{obs}}_{\mathrm{SKKS-SKS}} - T^{\mathrm{REF}}_{\mathrm{SKKS-SKS}},$$

where $T^{\mathrm{obs}}_{\mathrm{SKKS-SKS}}$ is the observed differential travel-time between SKKS and SKS, and $T^{\mathrm{REF}}_{\mathrm{SKKS-SKS}}$ is the predicted differential travel-time from a reference model. In this study, we use either the PREM or *S*-wave tomography model TXBW (Grand, 2002) as the reference model. We define the amplitude ratios as

$$\delta A_{\mathrm{SKKS}} = \log_{10}\left(\frac{A_{\mathrm{SKKS}}}{A_{\mathrm{SKS}}}\right)^{\mathrm{obs}} - \log_{10}\left(\frac{A_{\mathrm{SKKS}}}{A_{\mathrm{SKS}}}\right)^{\mathrm{PREM}},$$

where A_{SKKS} and A_{SKS} are the amplitudes of the SKKS and SKS arrivals in either our observations or in PREM predictions. Amplitude measurements are all based on PREM synthetics as we do not compute synthetics through tomography model TXBW for each observation in which to make an amplitude estimate. In this study, we do not measure differential travel-times using a cross-correlation as was done in previous studies. Rather, we measure differential travel-times based on peak times which provides greater sensitivity to ULVZ structures. We measure the SKS peak in a ±20 s window centered on the PREM prediction. We measure SKKS peaks within −5 and +20 s from the PREM prediction, after the seismogram has been phase shifted by $3\pi/2$ to account for the SKKS phase shifts.

A synthetic example is shown in Figure 2. Here we show displacement synthetic seismograms for a 500 km deep earthquake computed with the PSVaxi method (Jahnke, 2009; Jensen et al., 2013; Thorne, Garnero, et al., 2013). The PSVaxi technique is a 2-D finite difference method for computing synthetic seismograms in axi-symmetric geometries. The seismograms are split into two parts as either normal displacement (red and black traces in the vicinity of SKS) or $3\pi/2$ phase shifted displacement (gray and orange traces in the vicinity of SKKS). PREM synthetics are shown in black (near SKS) and gray (phase shifted, near SKKS). The ULVZ synthetics are shown in red (near SKS) and orange (phase shifted, near SKKS). The model shown is a 30 km thick box-car shaped ULVZ with a length (l) of 2.7° (164 km on the CMB) in the great-circle arc direction, that starts 15.0° in angular distance from the source.

First, we will describe the travel-time behavior shown in this example. The peak arrival in the ULVZ synthetic seismograms is indicated by the red asterisk. At the shortest epicentral distances (∼100°–107°) the peak arrival in the SKS window is increasingly delayed for the ULVZ model with respect to PREM, whereas the SKKS arrivals in PREM and the ULVZ model are not significantly altered. This shows up as decrease in δT_{SKKS}. Between ∼108° and 111°, we see that the SKS arrival has clearly bifurcated into two arrivals, with the second arrival having the largest amplitude and thus the peak time is picked on the second arrival. The second arrival in this window is related to the SPdKS arrival, but likely occurs due to a conversion of the down-going *S*-wave to a *P*-wave at the boundary of the ULVZ which creates a second P_{diff} arrival traveling ahead of SPdKS (Thorne et al., 2020). This manifests as a continuation of the decrease in δT_{SKKS}, which reaches its minimum value at 111°. At 112°, the first arrival in the SKS window has the largest amplitude, which causes an abrupt jump in δT_{SKKS}. From approximately 112°–125°, there is only a small difference in δT_{SKKS}.

The amplitude behavior of SKS and SKKS was first described in a theoretical study by Choy (1977). Our primary observation is the increase in δA_{SKKS} that peaks around 108°–109°. This increase in δA_{SKKS} has previously been observed in data for the central Pacific region and was interpreted in terms of ULVZ presence (Y. Zhang et al., 2009). In PREM when the SPdKS phase is initiated, some of the energy in the down-going *S*-wave gets converted to P_{diff}, and the subsequent SKS arrival loses some of its energy to SPdKS. This appears as a large increase in the SKKS amplitude relative to SKS at the emergence of SPdKS (see synthetic seismogram for PREM at 111°, Figure 2a). In the ULVZ model, energy in the SKS arrival is lost at an earlier epicentral distance because the down-going *S*-wave interacts with the ULVZ before SPdKS is initiated. This

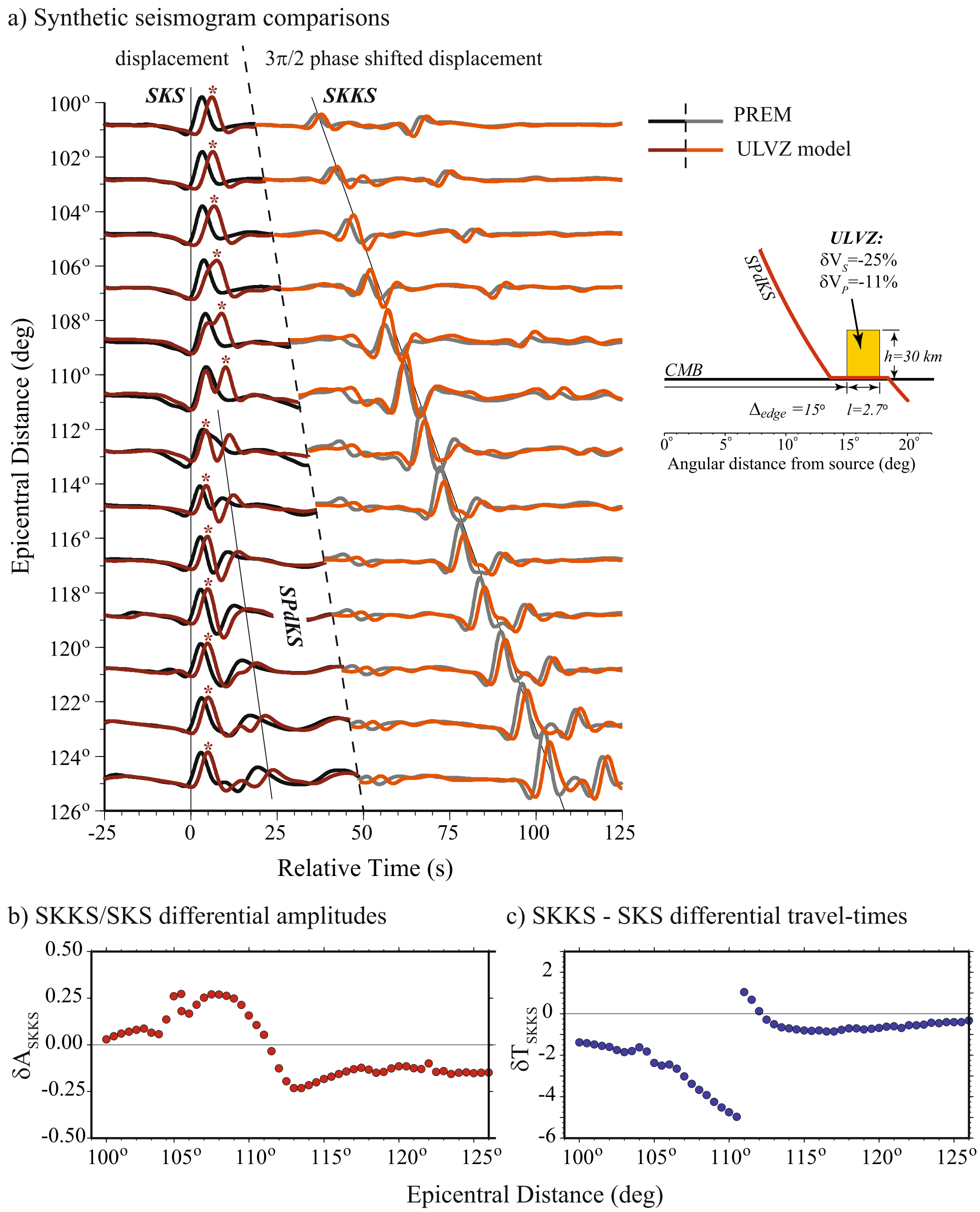

Figure 2. (a) Comparison of synthetic seismograms for PREM and an ultralow-velocity zone (ULVZ) model. The ULVZ model has $\delta V_S = -25\%$, $\delta V_P = -11\%$, thickness (h) = 30 km, length in the great circle arc direction $l = 2.7°$, and a ULVZ edge location $\Delta_{\text{edge}} = 15.0°$. A schematic drawing of the ULVZ model is shown in the inset to the right of the panel with a SPdKS raypath drawn at an epicentral distance of 108° for reference. The seismograms are broken in two as follows: (1) on the left, displacement seismograms are shown aligned on the PREM predicted arrival time for SKS and normalized to unity on the peak amplitude within a 25 s time window after the predicted SKS arrival time. The black traces are for PREM and the red traces are for the ULVZ model. The peak of the ULVZ model traces is indicated with a red asterisk. Synthetic seismograms are bandpass filtered with corners between 6 and 40 s; (2) on the right, $3\pi/2$ phase shifted displacement traces are shown. These traces are phase shifted from the amplitude normalized traces on the left. The gray traces are for PREM and the orange traces are for the ULVZ model. (b) The differential amplitude of SKKS with respect to SKS is shown for the ULVZ model relative to the PREM model. (c) The differential travel-time of SKKS with respect to SKS is shown for the ULVZ model relative to the PREM model. CMB, core-mantle boundary.

causes the amplitude of SKKS relative to SKS to spike at an earlier epicentral distance than in PREM as is observed in the δA_{SKKS} measurements in Figure 2b.

Note that the example shown in Figure 2 represents a special case in which the SPdKS arrival emerges with an amplitude that is larger than that of SKS. Observations similar to this, with large emergent SPdKS amplitudes, are common in a variety of geographic settings (Thorne et al., 2020). In this case, the peak amplitude at the shortest epicentral distances is due to the combined SKS + SPdKS arrivals. But, as SPdKS moves out with respect to SKS, the SPdKS arrival is the sole arrival being picked in the measurement. As SPdKS continues to move out, its amplitude gradually decreases until the SPdKS amplitude drops below that of SKS. At this point, the peak amplitude in the search window suddenly shifts to the SKS arrival and we observe a sudden shift in δT_{SKKS}. This travel-time behavior is most distinctive for ULVZ models where SPdKS emerges with a larger amplitude than SKS, however not all ULVZ models produce SPdKS arrivals with such large amplitudes. When the SPdKS arrival emerges with an amplitude smaller than that of SKS, the δT_{SKKS} curve does not contain the discontinuous jump around 112°. In these cases, the peak amplitude at the shortest epicentral distances is still the combined SKS + SPdKS arrivals, which may look delayed relative to SKS by itself in PREM. But, at the larger distances SKS, and not SPdKS, is the only arrival that is tracked. Thus, as SPdKS moves out, there is not a sudden jump in δT_{SKKS}.

3.2. Data Measurements

In order to apply this measurement technique to the real data, a few additional considerations must be made. Data measurements are made relative to PREM synthetics. We created a database of PREM synthetic seismograms for events in depths from 300 to 650 km in 25 km increments, and in epicentral distances from 100° to 130° in 0.5° increments using the PSVaxi method. Each data trace is compared to the closest synthetic in depth and distance. As described in Thorne et al. (2020) an empirical SKS wavelet was constructed for each event by stacking SKS records in the distance range from 90° to 105° and finding the best-fit triangle or truncated triangle function by grid search which could subsequently be used to convolve with the PREM synthetics before comparison. Initially, we made our travel-time measurements relative to the PREM model. But, as shown in Thorne, Zhang, and Ritsema (2013) the presence of the Pacific LLVP adds additional travel-time anomalies between SKKS and SKS, so we also made our travel-time measurements with respect to tomography using the model TXBW as the reference model (Grand, 2002). Tomographic travel-times were measured by tracing rays in PREM using the Tau-P Toolkit (Crotwell et al., 1999) and overlaying these on the tomography model to sum the travel-time. We first experimented with 3-D ray tracing using the LLNL-Earth3D package (Simmons et al., 2012). However, this method added considerable scatter to our observations (see Figure S40), so we simply used the 1-D ray tracing approach described above. As there is negligible difference between 1-D and 3-D rays for SKS and SKKS for these paths choice in tomography model makes little difference in the pattern of δT_{SKKS} (see Figures S39 and S41). δA_{SKKS} measurements were corrected to account for the axi-symmetric ring-source radiation pattern introduced by the PSVaxi method in the PREM synthetics and for the data using moment tensor solutions from the USGS catalog. δT_{SKKS} and δA_{SKKS} measurements for each event were ultimately grouped and averaged in 0.5° epicentral distance bins for comparison with synthetics as described in Section 5.3.

3.3. Comparison With Synthetics

We compare δT_{SKKS} and δA_{SKKS} measurements from the data to those of 2.5D synthetic seismograms computed for ULVZ models. We consider box-car shaped ULVZ models where we fix the density contrast ($\delta\rho$) at +10% commensurate with density constraints from other studies (Brown et al., 2015; Rost et al., 2005). We allow five ULVZ parameters to vary: (a) δV_S, (b) δV_P, (c) h—ULVZ thickness, (d) l—ULVZ length in the great circle arc direction, and (e) Δ_{edge}—angular distance to the leading edge of the ULVZ. For selected events, we perform a line minimization where we select a starting model, and then compute synthetics for perturbations to that model one parameter at a time. We calculate the data to synthetic misfit as follows. First, we calculate the sum of the squared residuals in δT and δA between the data and ULVZ model separately. This is done for the starting model and each perturbation to that model. Then we use an equally weighted linear combination of misfits from the model and each perturbation, where each is scaled to range from 0 to 1. At each step, we update the model to the perturbation with the lowest misfit, if no perturbation produces a lower misfit, then we retain the original model and move on to the next ULVZ parameter. Because static offsets exist in the measurements of δT_{SKKS} and δA_{SKKS}, we also include a parameter in our inversion to account for the offset. Thus, in our inversions, we are fitting the δT_{SKKS} and δA_{SKKS} patterns and not the absolute values which depend on the larger-scale 3-D seismic structure which we cannot perfectly account for using tomographic models.

At first, we use a large range and step-size of ULVZ parameter perturbations. For example, we start with δV_S ranging from −5% to −50% in 5% increments. At later iterations, we reduce the range and step-size of the perturbations (e.g., ±10% in 1% increments for δV_S). We continue the line minimization until no change in ULVZ parameter reduces the misfit.

A starting model is chosen by comparison of the data to synthetics for a bank of 306 ULVZ models. The model bank was created to coarsely span the range of possible ULVZ parameters. Parameters ranged from: (a) δV_S varied from −40% to −10% in 10% increments, (b) δV_P varied from −40% to −10% in 10% increments, (c) h was allowed to be 10, 20, or 40 km, (d) l was allowed to be 3°, 6°, or 12°, and (e) Δ_{edge} was allowed to be 8°, 11°, 14°, 17°, or 20°. The model with the lowest misfit relative to the event data was chosen as the starting model.

4. Results

4.1. Data Measurements

Data and measurements for one of the cleanest events (event #6 in Table 2 occurring on May 4, 2014) are shown in Figure 3. This event has several highly anomalous SPdKS records as identified in Thorne et al. (2020) which are evident in the data stacks (Figure 3a) for distances between 109° and 112°. Here we see SPdKS-like arrival emerging from SKS with a larger amplitude than SKS, reminiscent of the synthetics shown in Figure 2. This is manifest in the δA_{SKKS} measurements by an increase in the amplitude ratio at distances less than approximately 113°. We see a steady decrease in δT_{SKKS} reaching a minimum of about −4 s at a distance of 113°. Despite using records at a wide range of azimuths (30°–70°, see Table 1) the measurements are consistent and a pattern is observed similar to those of the synthetics in Figure 2.

The event closest to the May 4, 2014 event in our data set occured on June 17, 2017 (Event #10 in Table 2). The epicenters of these events are only separated by 0.7° (78 km). Data and measurements for this event are shown in Figure 4. Although records for #10 do not have as high of a signal-to-noise ratio as the 2014 event, there is remarkable agreement in the pattern of δT_{SKKS} and δA_{SKKS} between the two events. Although we note a static offset in the amplitude measurements between the two events, this demonstrates that two nearby events display nearly identical waveform shape and measurements of differential travel-times and amplitudes.

Another high-quality event is shown in Figure 5 (Event #9 in Table 2, February 24, 2017). This event epicenter is located 3.8° to the northeast from the May 4, 2014 event shown in Figure 3, however the average raypath azimuth is almost identical for these events. δT_{SKKS} and δA_{SKKS} measurements show a pattern remarkably similar to the two examples discussed above. Note that this event occurred at a depth of 414 km which is on the order of 100 km more shallow than the previous two events (527 and 511 km respectively), but shows distinctly similar waveforms and anomalies in travel-time and amplitude. Hence, it is unlikely that near source structure is responsible for these anomalous observations.

Other nearby events (events #1, #2, and #11) all show similar patterns in δT_{SKKS} and δA_{SKKS} as the events discussed above (events #6, #9, and #10). We will refer to this as pattern A. Of the remaining events, event #8 appears somewhat similar to pattern A, but the pattern is less clear for this event. Events #12 and #13 have their Pd arcs the furthest to the northeast. Their travel-times are somewhat similar to pattern A, yet the amplitudes are nearly flat and almost PREM-like. Events #4, #5, and #7 show complex waveforms and complex measurments of δT_{SKKS} and δA_{SKKS} that are difficult to interpret. These events have paths that are parallel to those of events #6 and #10, but are further away. δT_{SKKS} and δA_{SKKS} measurements for all events are provided in the online supplements.

Event #3 is unique and is shown in Figure 6. The shape of δA_{SKKS} is similar to pattern A except the peak in the amplitude ratios appears to be shifted to slightly larger epicentral distances. However, δT_{SKKS} appears to climb in the distance range from 100° to 112° rather than decrease as in the case of pattern A. This event is located further to the southwest of event #6, and thus it may be encountering a ULVZ at a greater Δ_{edge}.

10.1029/2021JB021897

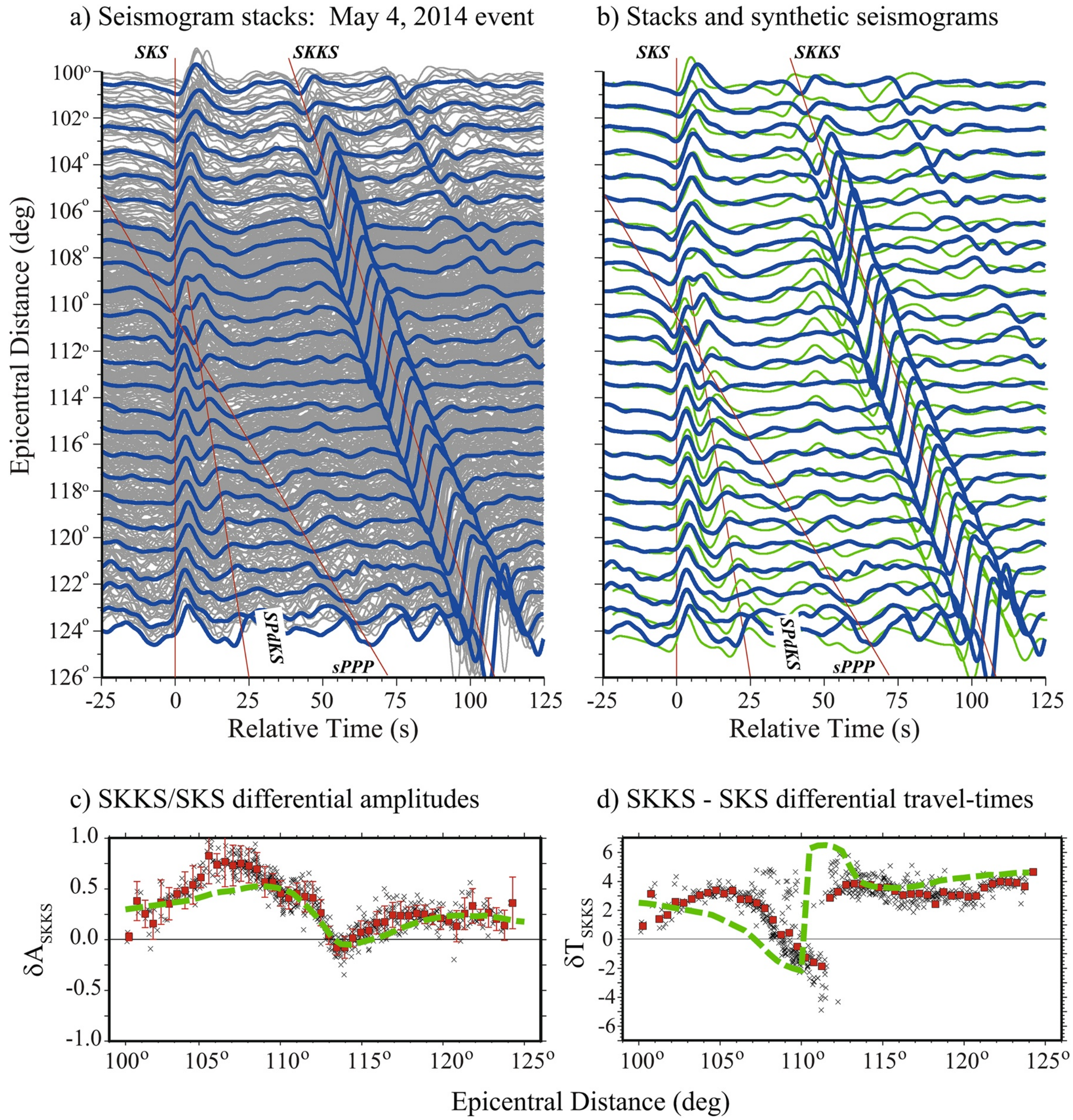

Figure 3. (a) Radial component displacement seismograms for the May 4, 2014 event (Event #6 in Table 2). All seismograms are aligned in time on the PREM predicted SKS arrival time and normalized to unity on the peak amplitude from 0 to 20 s. Seismograms are shown in the azimuth range from 30° to 70°. Individual seismograms are drawn in gray and stacks in 1° epicentral distance bins are drawn in blue. (b) Seismogram stacks are repeated in blue and overlain for synthetics (green) computed for a ultralow-velocity zone model with $\delta V_S = -20\%$, $\delta V_P = -15\%$, $h = 26$ km, $\Delta_{\mathrm{edge}} = 8.5°$, and length ($l$) = 10.0°. (c) Differential amplitude measurements, δA_{SKKS}, for the event are shown. Measurements for each trace are shown with black crosses. The red squares and error bars show averages and one standard deviation error bars in 0.5° epicentral distance bins. The dashed green line shows the synthetic prediction for the model shown in the previous panel. (d) Differential travel-time measurements, δT_{SKKS}, corrected for tomography. Measurements for each trace are shown with black crosses. The red squares and error bars show averages and one standard deviation error bars in 0.5° epicentral distance bins. The dashed green line shows the synthetic prediction.

4.2. Synthetic Modeling

Finding ULVZ models that explain these data are performed using line minimization. We initiate the search from one of the models in our coarse synthetic model bank. Figure 7 shows travel-time predictions (δT_{SKKS}) for a subset of these models. In this figure we show how δT_{SKKS} varies as function of ULVZ size (h, l, and Δ_{edge}) where δV_s and δV_P are both held constant at −20%. Only a limited number of models reproduce the travel-time variation pattern as observed for the data with a pattern A. For example, a model with length

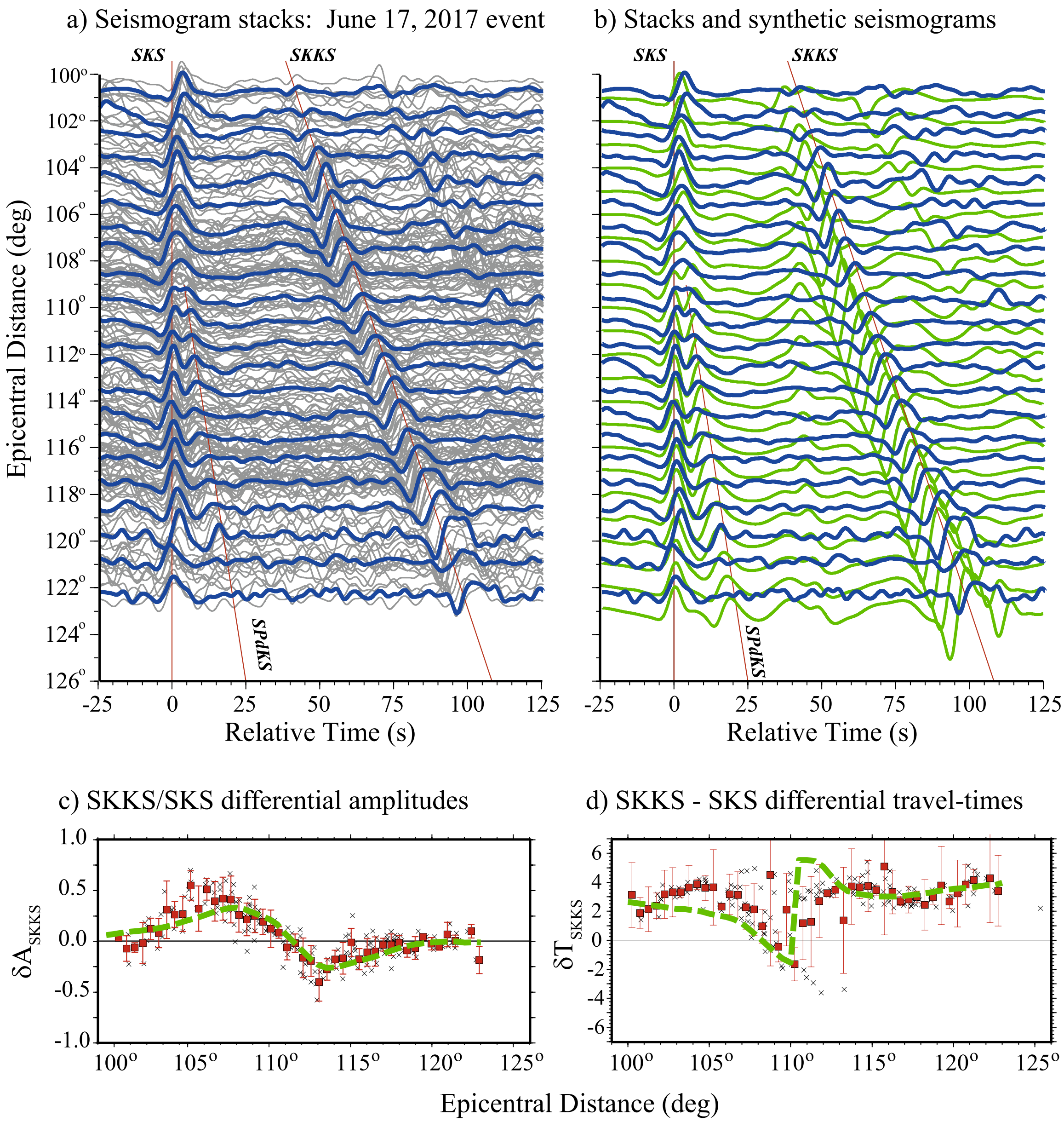

Figure 4. (a) Seismograms for the June 17, 2017 event (Event #10 in Table 1). Seismograms are shown in the azimuth range from 40° to 70°. (b) Seismogram stacks are repeated in blue and overlain for synthetics (green) computed for a ultralow-velocity zone model with $\delta V_S = -20\%$, $\delta V_P = -15\%$, $h = 26$ km, $\Delta_{\text{edge}} = 8.5°$, and length ($l$) = 10.0°. (c) Differential amplitude measurements, δA_{SKKS}, for the event are shown. (d) Differential travel-time measurements, δT_{SKKS}, corrected for tomography.

(l) = 3°, $\Delta_{\text{edge}} = 14°$, and $h = 40$ km (third row of column a in Figure 7) has a similar travel-time pattern as a model with length (l) = 6°, $\Delta_{\text{edge}} = 11°$, and $h = 40$ km (second row of column b in Figure 7). That is, we observe a fundamental trade-off between ULVZ length and position. Seismograms that produce the pattern A travel-time anomaly are typically associated with the highly anomalous type of waveforms as described in Thorne et al. (2020). Thus, we can infer that from travel-time observations alone, and perhaps waveform shape of SPdKS, it may not be possible to constrain ULVZ size and position.

δT_{SKKS} is moderately sensitive to the ULVZ position. For example, consider the model with length (l) = 6°, $\Delta_{\text{edge}} = 11°$, and $h = 10$ km (second row of column b in Figure 7). Here we see the pattern A travel-time behavior. However, if the ULVZ position is shifted 3° further away to the model with length (l) = 6°, $\Delta_{\text{edge}} = 14°$, and $h = 10$ km (third row of column b in Figure 7) the pattern shifts to one where we see δT_{SKKS}

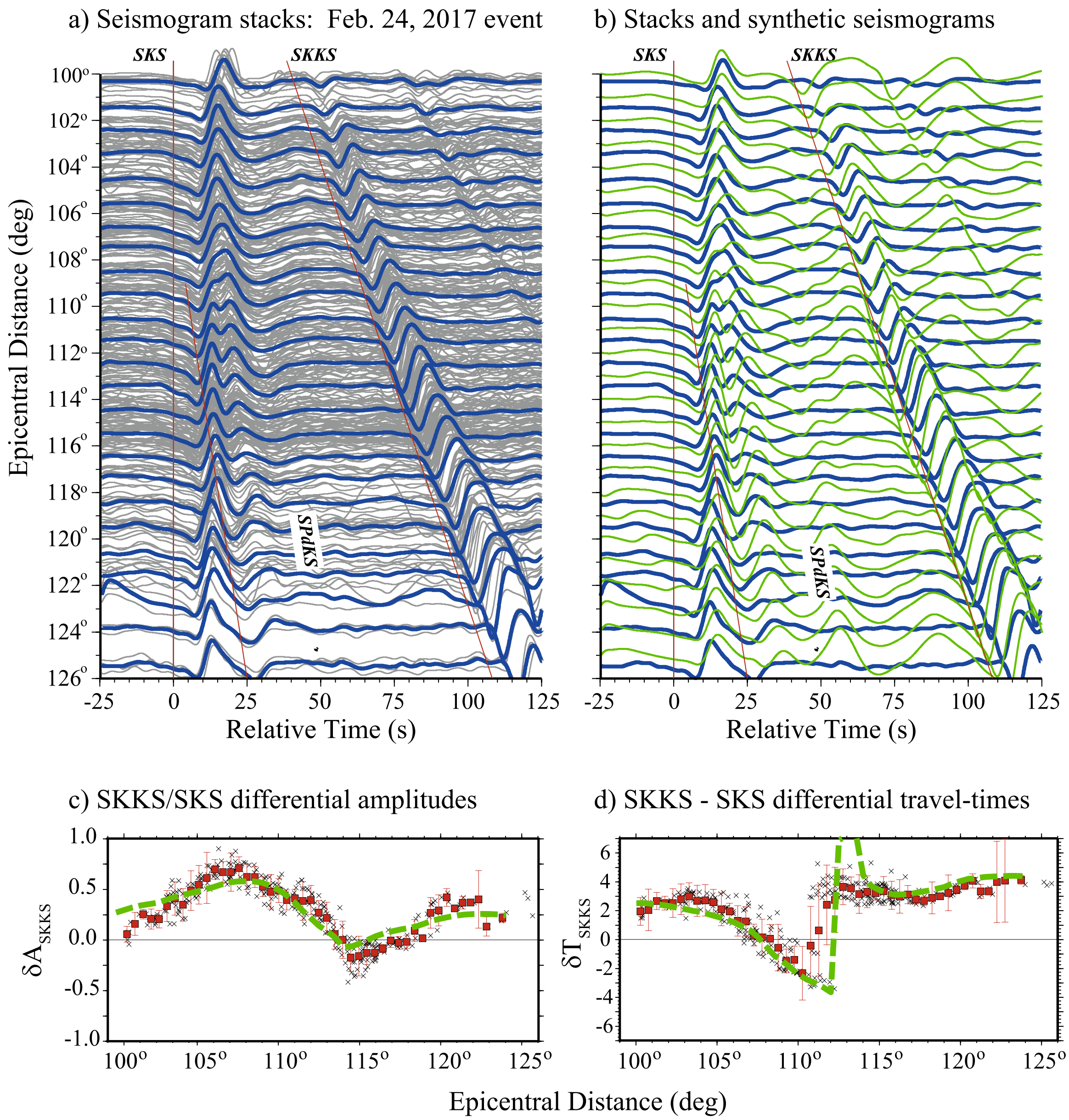

Figure 5. (a) Seismograms for the February 24, 2017 event (Event #9 in Table 2). Seismograms are shown in the azimuth range from 30° to 70°. (b) Seismogram stacks are repeated in blue and overlain for synthetics (green) computed for a ultralow-velocity zone model with $\delta V_S = -20\%$, $\delta V_P = -17\%$, $h = 26$ km, $\Delta_{\mathrm{edge}} = 8.75°$, and length ($l$) = 10.75°. (c) Differential amplitude measurements, δA_{SKKS}, for the event are shown. (d) Differential travel-time measurements, δT_{SKKS}, corrected for tomography.

increase at the epicentral distances less than roughly 112°. This is similar to the pattern we observed for event #3 (Figure 6).

Figure 8 shows amplitude predictions (δA_{SKKS}) for the same ULVZ models as shown in Figure 7. Here we can see that, although a model with length (l) = 3°, $\Delta_{\mathrm{edge}} = 14°$, and $h = 40$ km may have fit the travel-times well for event #6 (Figure 3), it severely under-predicts the increase in amplitude ratios. In particular, we can see that for event #6 the peak-to-peak change in δA_{SKKS} is on the order of 0.8 (Figure 3), whereas the peak-to-peak change in δA_{SKKS} is on the order of 0.4 for the length (l) = 3° synthetics in Figure 8. But, increasing the size of the ULVZ has the tendency to increase the amplitude ratio. And thus to fit both travel-times and amplitudes for event #6, we need to increase its size. For example, a model with length (l) = 12°, $\Delta_{\mathrm{edge}} = 8°$, and $h = 20$ km (green line in first row of column c in Figure 8).

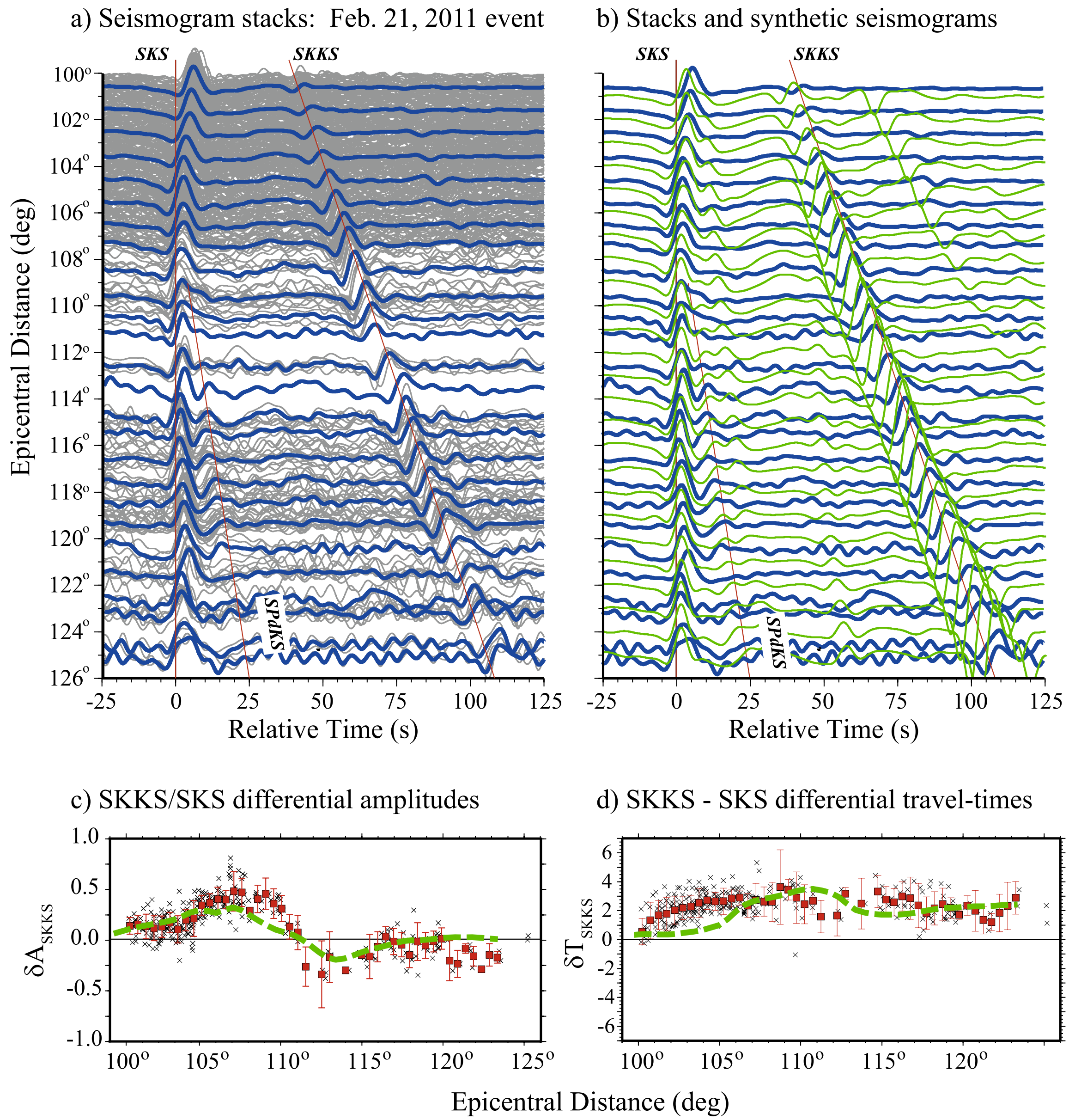

Figure 6. (a) Seismograms for the February 21, 2011 event (Event #3 in Table 2). Seismograms are shown in the azimuth range from 30° to 70°. (b) Seismogram stacks are repeated in blue and overlain for synthetics (green) computed for a ultralow-velocity zone model with $\delta V_S = -20\%$, $\delta V_P = -15\%$, $h = 26$ km, $\Delta_{\text{edge}} = 13°$, and length ($l$) = 10.0°. (c) Differential amplitude measurements, δA_{SKKS}, for the event are shown. (d) Differential travel-time measurements, δT_{SKKS}, corrected for tomography.

We performed a line minimization of events #6 and #9 which showed the cleanest signal in δT_{SKKS} and δA_{SKKS}. For event #9, we initiated the search for model with $\delta V_S = -20\%$, $\delta V_P = -20\%$, $h = 30$ km, $l = 12°$, and $\Delta_{\text{edge}} = 8°$. After 15 iterations, we converged on a best-fit model with $\delta V_S = -22\%$, $\delta V_P = -17\%$, $h = 26$ km, $l = 10.75°$, and $\Delta_{\text{edge}} = 8.75°$. Similarly for event #6, we found a best-fit model with $\delta V_S = -20\%$, $\delta V_P = -15\%$, $h = 26$ km, $l = 10.0°$, and $\Delta_{\text{edge}} = 8.5°$. Synthetic seismograms for these models and events are shown in comparison to data stacks for these events in Figures 3b and 5b. Comparison of synthetic predicted δT_{SKKS} and δA_{SKKS} are also shown in Figures 3c, 3d, 5c and 5d. Because events #6 and #10 were nearly co-located, we also show predictions for the best-fit model (for event #6) in comparison to event #10 in Figures 4b–4d.

In each of the cases shown above (Figures 3–5), the general character of the δT_{SKKS} and δA_{SKKS} measurements are well represented. However, the model and observation misfit are not perfect. This is likely due to

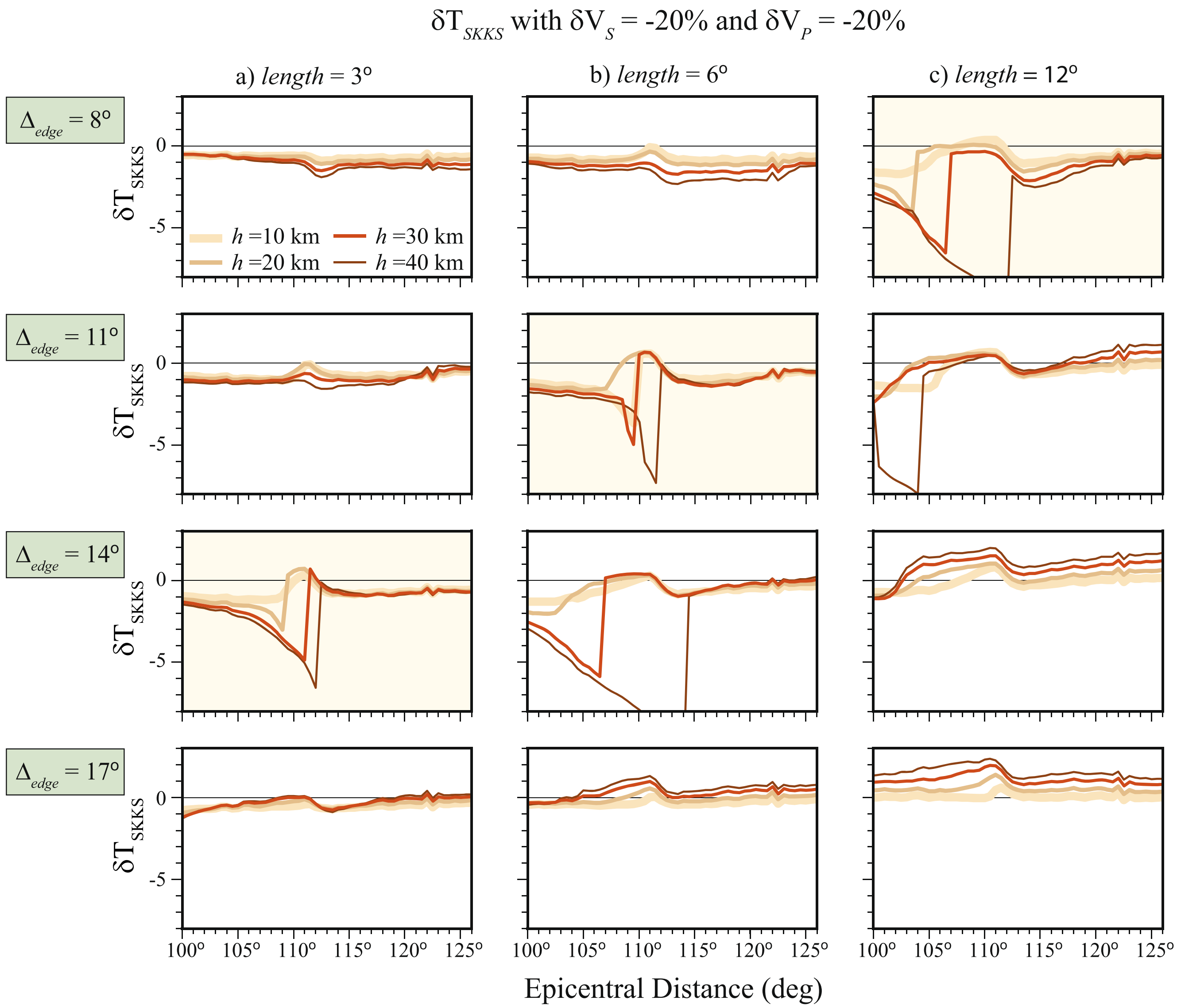

Figure 7. Synthetic predictions of δT_{SKKS} for select ultralow-velocity zone (ULVZ) models. All models shown have $\delta V_S = -20\%$ and $\delta V_P = -20\%$. Each column shows a ULVZ with a length in the great circle arc direction of (a) $l = 3°$, (b) $l = 6°$, and (c) $l = 12°$. Each row shows a ULVZ with an edge position of: (row 1) $\Delta_{\mathrm{edge}} = 8°$, (row 2) $\Delta_{\mathrm{edge}} = 11°$, (row 3) $\Delta_{\mathrm{edge}} = 14°$, (row 4) $\Delta_{\mathrm{edge}} = 17°$. Each panel shows the prediction for four different ULVZ heights, h = 10, 20, 30, and 40 km ranging from light to dark brown. Panels highlighted in yellow have models that are potentially compatible with observations for events #6 and #10 shown in Figures 3 and 4.

trying to fit a 3-D structure with a 2-D axisymmetric model, and also the fact that we are only using simple box-car shaped models. Nonetheless, using the axisymmetric approach used here, we are unable to find a reasonable fit to both δT_{SKKS} and δA_{SKKS} without using the large-scale ($l = 10.0°$ or greater) ULVZ models.

We can also see that the predicted SKKS arrival is not always as delayed for the ULVZ model as is observed in real data (see Figures 3b and 4b). In conducting our line minimization, we also inverted for a static shift between the observations and model, which often was as large as 4 s. The need to invert for this static shift is likely because of large-scale *S*-wave velocity perturbations that are not accounted for in tomography. Even though we corrected travel-time measurements for a tomographic model (model TXBW), this model did not erase all of the large-scale travel-time perturbations. This problem has been explored in past studies and in particular, it is already known that tomography models underpredict travel-time delays for seismic phases crossing the Pacific LLVP (Thorne, Zhang, & Ritsema, 2013).

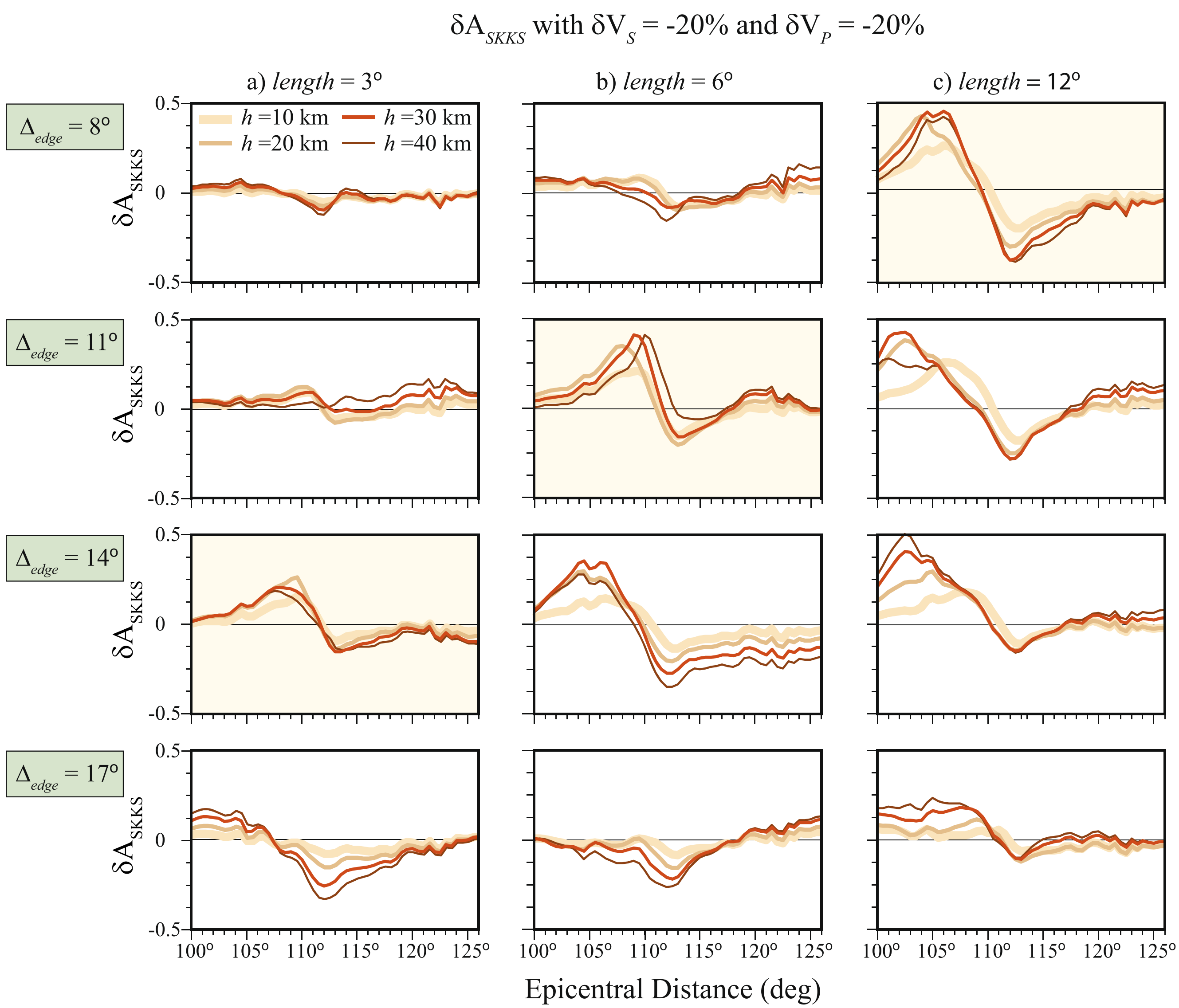

Figure 8. Synthetic predictions of δA_{SKKS} for select ultralow-velocity zone (ULVZ) models. All models shown have $\delta V_S = -20\%$ and $\delta V_P = -20\%$. Each column shows a ULVZ with a length in the great circle arc direction of (a) $l = 3°$, (b) $l = 6°$, and (c) $l = 12°$. Each row shows a ULVZ with an edge position of: (row 1) $\Delta_{\mathrm{edge}} = 8°$, (row 2) $\Delta_{\mathrm{edge}} = 11°$, (row 3) $\Delta_{\mathrm{edge}} = 14°$, (row 4) $\Delta_{\mathrm{edge}} = 17°$. Each panel shows the prediction for four different ULVZ heights, $h = 10$, 20, 30, and 40 km ranging from light to dark brown. Panels highlighted in yellow have models that are potentially compatible with observations for events #6 and #10 shown in Figures 3 and 4.

The event #3 epicenter is located 1.6° to the southwest of event #6. If the best-fit ULVZ position for event #6 is correct, we would expect the Pd rays to encounter this ULVZ at a larger Δ_{edge} position. Hence we computed synthetic predictions for this best-fit model ($\delta V_S = -20\%$, $\delta V_P = -15\%$, $h = 26$ km, $l = 10.0°$) for a variety of Δ_{edge} positions to see if a larger position fits these data as we expected, finding that a Δ_{edge} position of 13° fits these data the best (Figures 6c and 6d). This best-fit model predicts δA_{SKKS} reasonably well, and predicts the general shape in δT_{SKKS} but does not capture the rapid rise in δT_{SKKS} at the shortest epicentral distances.

The better fit for event #6 with a larger Δ_{edge} position is evidence that we have the size and position of the ULVZ correct; however, we note that a larger distance of separation is found between events #6 and #9, than #6 and #3 and we do not see a comparable shift in position between the best-fit models for those two events. Comparison of best-fit ULVZ positions for these four events is shown in Figure 9. We note that this modeling was done with a 2D axi-symmetric geometry, hence the ULVZ positions indicated in Figure 9 are

10.1029/2021JB021897

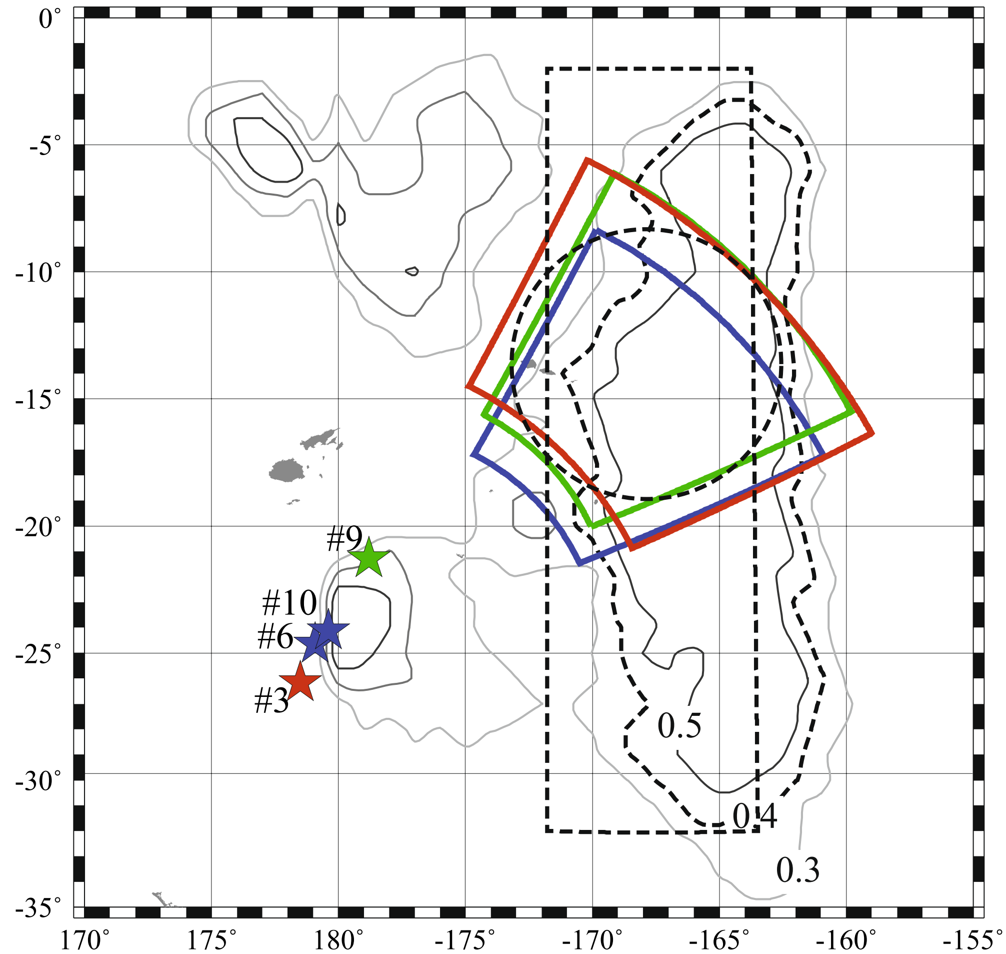

Figure 9. Modeled ultralow-velocity zone (ULVZ) locations for events #3, #6, #9, and #10. Event locations are indicated with stars and labeled by event number. ULVZ probability contours of 0.3 (light gray), 0.4 (gray), and 0.5 (dark gray) are reproduced from Thorne et al. (2021). Inferred ULVZ locations for each event are shown for event #3 (red line corresponding with red star for event #3), events #6 and #10 (purple line), and event #9 (green line). Regions are outlined based on the axi-symmetric geometry used in the waveform modeling and the azimuthal range of the data used (see Table 2). 3-D modeled areas shapes are indicated by dashed black lines for the boundaries of the 3-D rectangular ULVZ model, the 0.4 probability contour and the cylindrical shaped model described in Section 5.

drawn as the sectors of a circle where the azimuthal bounds are defined by the azimuthal bounds of the data used for each event (see Table 2) and the width of the ring is defined by the leading ULVZ boundary at Δ_{edge} and the far ULVZ boundary at $\Delta_{edge} + l$. Overall there is good overlap between these models, and they also overlap the ULVZ probability calculations of (Thorne et al., 2021). However, as seen from the probability contours, the Samoa ULVZ has a 3-D structure that the 2-D axi-symmetric modeling is not capturing. We will discuss possible 3-D effects in the next section.

5. Discussion

If a single large ULVZ is responsible for our observations, then we infer a maximum width of 10.75° (650 km along the CMB) when modeling in 2-D. However, the data used in this study appear to obliquely cross the Samoa ULVZ inferred in Thorne et al. (2021), so the actual ULVZ width may not be this large. This previous work inferred a long linear ULVZ stretched out in the North-South direction. We show probability contours of 0.4 and 0.5 from Thorne et al. (2021) in Figure 1 which are consistent with the ULVZ imaged here. However, our 2-D modeling efforts are averaging the 3-D structure. If the contours are a guide then we may be underestimating the ULVZ width for the smaller azimuths and overestimating the width for the larger azimuths. Nonetheless, if we are sampling the ULVZ obliquely then the actual width of the Samoa ULVZ may only be on the order of 8° (485 km) in the East-West direction if we use the 0.4 or 0.5 probability contours as a rough guide for the ULVZ shape.

Previous studies have suggested the Samoa ULVZ is between 250 and 400 km across (Thorne, Garnero, et al., 2013; Wen & Helmberger, 1998a). Here we suggest the ULVZ is likely at the larger end of that thescale approaching 500 km in width. Yet it is difficult to constrain as our ray paths may be crossing the ULVZ obliquely. But, given this constraint on ULVZ width in the raypath direction, this imposes limits on the ULVZ elastic parameters. Here we find that δV_S and δV_P reductions from 20% to 22% and 15% to 17% respectively gives us the best fit, for a ULVZ with a thickness of 26 km. Previously Thorne, Garnero, et al. (2013) proposed a larger *S*-wave velocity drop, as high as 45%. However, that study only considered 3:1 δV_S: δV_P ratios as implied by partial melt. In addition, that study did not use SKKS observations and also suggested a ULVZ that was not as wide as we model here. Thus, we do not disagree with the results of Thorne, Garnero, et al. (2013); rather that study just did not consider all the possibilities in the model space and also only considered SPdKS. As seen in Figures 3–5, the model we propose here also predicts the highly anomalous waveforms for this region that were modeled in Thorne, Garnero, et al. (2013). The results presented in this paper are also more consistent with previous SKKS and SKS based studies (Thorne, Zhang, & Ritsema, 2013; Y. Zhang et al., 2009) which both inferred a roughly 20 km thick ULVZ with a δV_S reduction between 20% and 30%.

It is now possible to compute short period (~2 s dominant period) synthetic seismograms for fully 3-D ULVZ models using the AxiSEM3D technique (Leng et al., 2019, 2020). This mixed pseudospectral/spectral-element method (Leng et al., 2016) exploits wavefield smoothness in the azimuthal direction, such that its discretization can be adapted to the complexity of the problem. For any 3-D models exhibiting regions of smooth variations, such as in tomographic models, with localized complex structures, such as ULVZs, the computational speedup can be drastic while retaining exact solutions. Previous tests conducted for a cylindrical ULVZ in 3-D compared with an axi-symmetric ULVZ in 2-D showed marked differences in predictions for the same base ULVZ model (Thorne et al., 2021). In that case, the cylindrical symmetry of the ULVZ focused energy into the ULVZ in a way that was not seen for the 2-D model, resulting in much more anomalous waveform shapes with larger amplitudes for SPdKS related seismic phases. However, in this location we do not see a cylindrical shaped ULVZ but rather a long linear ULVZ. The geometry of the ULVZ observed here is not however axi-symmetric, and so we test the long linear ULVZ shape in 3-D relative to the 2-D axi-symmetric case.

In particular, we tested three 3-D geometries: (a) a rectangular shaped ULVZ that has a width constrained by our modeling of event #6 (modeled rectangle size is 9.2°×35°), (b) a cylindrical-shaped ULVZ that has a 10.75° diameter constrained by our modeling of event #6, and (c) an approximately rectangular NS elongate—irregularly shaped ULVZ defined by the 0.4 ULVZ probability contour of Thorne et al. (2021) (see Figure 9). For each of the three models, we used an *S*-wave velocity reduction of 20%, and *P*-wave velocity reduction of 15% and a thickness of 26 km as best-fit by event #6. The first model is tested in order to examine how well the axi-symmetric modeling compares to a fully 3-D model in this case where we have previously inferred that the ULVZ has a long linear shape. The second model is selected in order to assess whether the long linear shape is necessary. The third model is chosen to see how the irregularity of the boundary affects the wavefield and to test whether the probability contours of Thorne et al. (2021) may act as a reasonable proxy to the ULVZ shape. Thorne et al. (2021) compared 2-D axi-symmetric synthetics to a cylindrical 3-D ULVZ. The 3-D cylindrical ULVZ strongly focused energy and predicted much more anomalous waveforms than the 2-D case. Hence, our overall goal in these 3-D tests is to determine whether or not the ULVZ size and elastic parameters are over-estimated by the 2-D modeling we performed.

Results for the different 3-D models are shown in Figure 10. These synthetic seismograms are computed for source characteristics of event #6 (see Table 2). We computed synthetics at the same receiver locations used for this event and stacked them into 1° epicentral distances bins as was done with these data. Stacked synthetics (red traces) are compared to the stacked data (blue traces) in Figures 10a–10c. Visually, all three synthetic models compare reasonably well with the data, but differences exist in the 110°–111° distance range in which the timing and amplitude of the SPdKS arrival do not quite match up. A more quantitative comparison is made in Figures 10d and 10e in which the δA_{SKKS} and δT_{SKKS} measurements are shown. Little

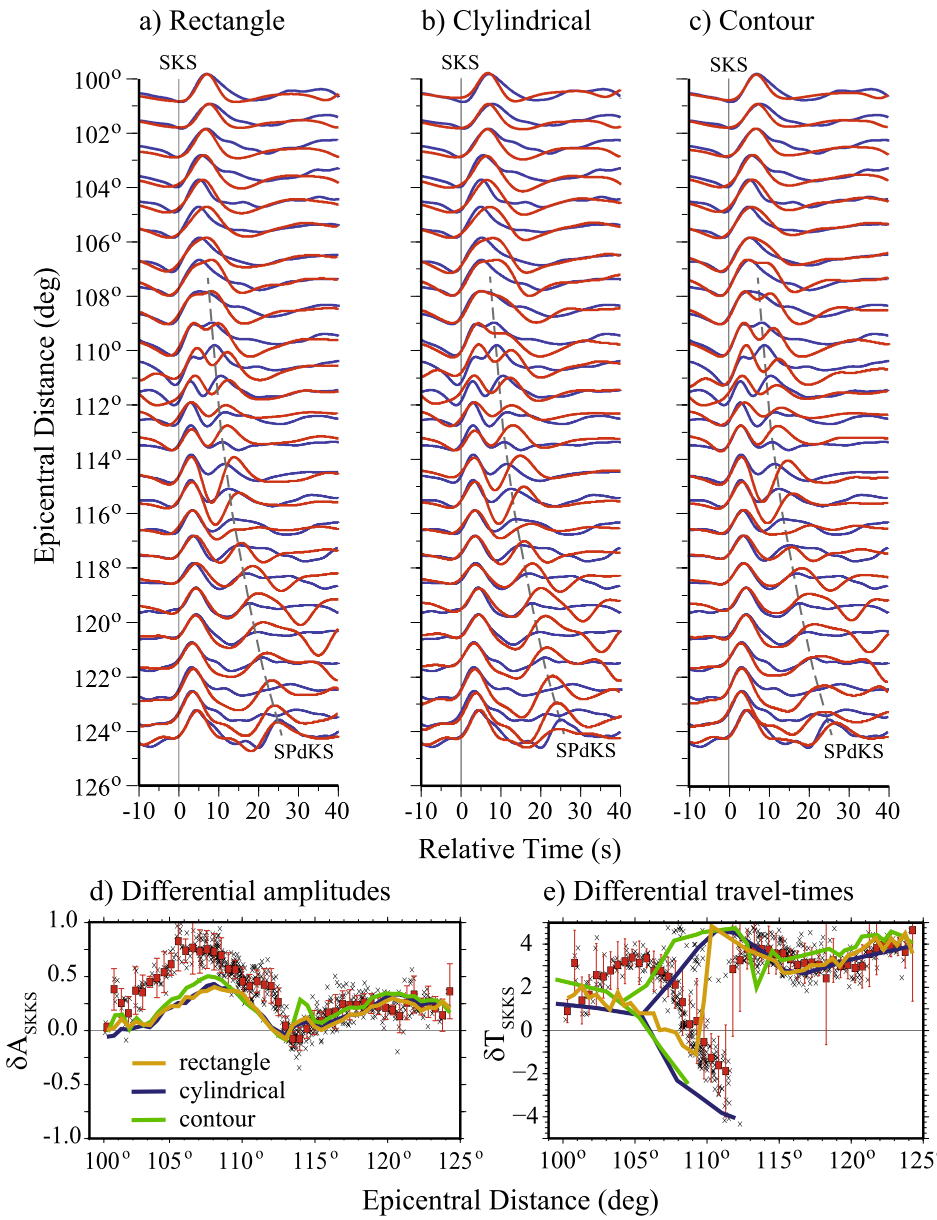

Figure 10. Data stacks for the May 4, 2014 event (Event #6 in Table 2) are given in blue. All traces are radial component displacement seismograms. 3-D synthetic seismograms are given in red for either (a) a rectangular approximation to the Samoa ultralow-velocity zone (see purple dashed line in Figure 9), (b) a cylindrical shaped approximation (see black dashed circle in Figure 9), or (c) the 0.4 probability contour (see solid purple line in Figure 9). Approximate SPdKS arrival is indicated by the dashed line. (d) δA_{SKKS} and (e) δT_{SKKS} measurements for the rectangle (orange), cylindrical (blue), and contour (green) 3-D synthetic models compared to data. Black crosses correspond to individual data measurements. The average and standard deviations are given by the red squares and lines.

variation is seen in the δA_{SKKS} measurements for the three models, and all three models underestimate the amplitude ratios at the shortest epicentral distances. The differential travel-times show much greater variation in the patterns than the amplitude measurements. The rectangle model shows the closest agreement with the data, although the minimum in δT_{SKKS} is not replicated. Both the cylindrical and contour models show a complicated multi-valued relationship. In both models, the observations for distances less than approximately 112° tend to split between regions where (a) δT_{SKKS} drops below zero and (b) δT_{SKKS} rises above zero. This split is due to the data being sampled over a wide azimuthal band and the complex behavior and sensitivity of the SPdKS waveforms with respect to ULVZ length (l) and edge positions (Δ_{edge}) as demonstrated in Figure 7. Interestingly, the data for events #4 and #5 that we did not try to model because of their complexity have δT_{SKKS} patterns suggestive of this split behavior which could be indicative of the 3-D nature of this ULVZ (see Figures S17 and S18).

Of the 3-D models, the rectangle model fits the observations the best as this model alone does not show a complex bi-modal distribution of travel-times in the 105°–113° epicentral distance range. However, discrepancy in both the amplitude and travel-time variations exists with respect to the data. We also computed 3-D models where we shifted the rectangle by one or two degrees in longitude to the east or west. Of the shifted models, a slight shift of 1° to the west provides a slightly better fit to these data. However, δA_{SKKS} is still underestimated and the magnitude of the δT_{SKKS} decrease is still not replicated. Both of these observations could be explained by the result of the different focusing observed in 2-D axi-symmetric versus 3-D synthetic seismograms for the SPdKS related phases (see supplemental animation in Thorne et al., 2021) as well as complex 3-D structure of the ULVZ.

Although we do not get a perfect agreement between models in 2-D and 3-D the results presented above suggest that the 2-D model results are generally consistent with 3-D models. The disagreement between 2-D and 3-D models could be due to the complex 3-D shape of the ULVZ and differences in focusing of the arrivals associated with SPdKS, both of which could affect the elastic parameters recovered. This demonstrates the importance of future efforts using a fully 3-D modeling. However, expanding the model space to 3-D geometries increases the possible model space dramatically and is beyond the scope of the present work.

Some additional considerations should be made with respect to the 2-D modeling used in this study. First, we only tested box-car shaped ULVZ models. Some previous efforts have suggested that ULVZs may be dome shaped or more irregularly shaped features (e.g., Wen & Helmberger, 1998a, 1998b). However, the ULVZ we image here has a thickness on the order of 20 km over a length of approximately 600 km in the great circle arc direction (the length is ~30× the height). Hence, the shape may not play as important of a role in our modeling as with other smaller-scale ULVZs, yet we did not test the effect of shape in this study. Furthermore, SPdKS has a complimentary phase SKPdS that occurs on the receiver-side of the path. Structure on the receiver-side of the path can also affect the waveforms we observe here. A large ULVZ is known to exist on the receiver-side beneath northern Mexico (Havens & Revenaugh, 2001; Spica et al., 2017; Thorne et al., 2019), but none of the Pd paths used in this study cross this ULVZ. However, we cannot rule out possible contamination from unknown ULVZs beneath N. America. But a previous effort has shown that the receiver-side effects are likely only observed on a handful of stations (Thorne et al., 2021). Since the patterns we observe in δT_{SKKS} and δA_{SKKS} are consistent over a large range of azimuths (a 30° or 40° span) it does not appear that a receiver-side structure is strongly affecting our measurements.

In addition to further 3-D modeling efforts, we may learn more about the Samoan ULVZ if we can incorporate additional seismic wave arrivals into the inversion. Unfortunately, there is little overlap in this region with the seismic phases most commonly used to detect ULVZs such as ScP (e.g., Rost & Revenaugh, 2003), ScS (e.g., Zhao et al., 2016), S_{diff} (e.g., Kim et al., 2020), and PKP (e.g., Waszek et al., 2015). However, additional information such as SPdKS back azimuth could provide additional constraints. Initial tests suggest that the circular ULVZ model shows significant energy coming from off great-circle path. In this study we do not attempt to measure whether the SPdKS energy is arriving from off great-circle paths, but future efforts could potentially use this as an additional constraint in fully 3-D waveform modeling efforts.

The elastic parameters we recovered with the 2-D modeling suggest a δV_S to δV_P ratio of 1.3, which is consistent with a compositional origin to the ULVZ (Brown et al., 2015; Wicks et al., 2010). From a geodynamic perspective, the most striking aspect of the Samoa ULVZ may be its long linear shape. Simulations show a similar snake-like shape when compositional ULVZ material is in the process of migrating across the CMB (Li et al., 2017; McNamara, 2019). When not in motion, compositional ULVZs appear rounded similar to the shape of most other inferred ULVZs (Thorne et al., 2021). However, the Samoa ULVZ lies directly in the center of the Pacific LLVP, and if this LLVP is a single feature such as a thermochemical pile as opposed to a tomographically blurred collection of mantle upwellings (Bull et al., 2009; Hosseini et al., 2019), then we expect the highest temperatures in the lowermost mantle to exist where we observe the Samoa ULVZ. Thus, it is possible that the Samoa ULVZ is composed of partial melt, a possibility which we cannot rule out based solely on the observed ULVZ size and shape in comparison to geodynamic simulations.

6. Conclusions

The long linear shape of the Samoa ULVZ appears unique among ULVZs that have been imaged to date. In this paper we considered measurements of both differential travel-times and amplitudes between SKKS and SKS, measurements which are highly sensitive to ULVZ properties and location as well as the emergence of the SPdKS arrival. Using these additional constraints, we observe that if a ULVZ is responsible for our observations then it must be on the order of 500 km wide or we are not able to predict the SKKS/SKS amplitude ratio measurements. In turn, the wider ULVZ implies that velocity variations for *S*- and *P*-waves are likely in the −20% and −15% range respectively. These velocity variations are more similar to a 1:1 δV_S: δV_P velocity ratio, and are consistent with a compositional origin to the ULVZ such as predicted for a ULVZ composed of highly Fe-enriched ferropericlase (Brown et al., 2015; Wicks et al., 2010). Interestingly, in geodynamic simulations a dense compositional anomaly in motion most resembles the shape of the Samoa ULVZ in our preferred model. Geochemical evidence points to a possibly ancient subduction component to the most recent volcanism in the Samoa line. Hence, if the ULVZ we observe beneath Samoa has material that is being entrained into Samoan hot spot lavas, these materials may in part be derived from ancient subduction (Jackson et al., 2014), which has been pushed to the central Pacific and is currently being entrained into the Samoa hot spot.

Data Availability Statement

All radial component displacement seismic recordings used in this study for the 13 events listed in Table 2 are freely available in the hive.utah.edu data repository: https://doi.org/10.7278/S50DT3X22GGB.

Acknowledgments

The authors are grateful for conversations with Allen McNamara which improved this manuscript. The authors thank Jenny Jenkins, the associate editor, and one anonymous reviewer for their extensive comments which greatly improved this manuscript. The authors acknowledge the University of Utah Center for High Performance Computing (CHPC) for computing resources and support. Michael S. Thorne and Justin Krier were partially supported by NSF grant EAR- 1723081. Justin Krier was also supported through the University of Utah Undergraduate Research Opportunities Program (UROP). Kuangdai Leng was fully supported by NERC grant NE/R012199/1. Tarje Nissen-Meyer were partially supported by NERC grant. Figures were drawn using the Generic Mapping Tools (Wessel & Smith, 1998).

References

Brown, S. P., Thorne, M. S., Miyagi, L., & Rost, S. (2015). A compositional origin to ultralow-velocity zones. *Geophysical Research Letters*, *42*(4), 1039–1045. https://doi.org/10.1002/2014gl062097

Bull, A. L., McNamara, A. K., & Ritsema, J. (2009). Synthetic tomography of plume clusters and thermochemical piles. *Earth and Planetary Science Letters*, *278*(3–4), 152–162. https://doi.org/10.1016/j.epsl.2008.11.018

Choy, G. L. (1977). Theoretical seismograms of core phases calculated by frequency-dependent full wave theory and their interpretation. *Geophysical Journal International*, *51*(2), 275–312. https://doi.org/10.1111/j.1365-246x.1977.tb06921.x

Cottaar, S., & Li, Z. (2019). *A large ultra-low velocity zone at the potential base of the Galapagos plume*. American Geophysical Union, Fall Meeting 2019, Abstract #DI33A-04. Retrieved from https://ui.adsabs.harvard.edu/abs/2019AGUFMDI33A.04C/abstract

Cottaar, S., & Romanowicz, B. (2012). An unsually large ULVZ at the base of the mantle near Hawaii. *Earth and Planetary Science Letters*, *355–356*, 213–222. https://doi.org/10.1016/j.epsl.2012.09.005

Crotwell, H. P., Owens, T. J., & Ritsema, J. (1999). The TauP Toolkit: Flexible seismic travel-time and ray-path utilities. *Seismological Research Letters*, *70*, 154–160. https://doi.org/10.1785/gssrl.70.2.154

Dziewonski, A. M., & Anderson, D. L. (1981). Preliminary reference Earth model. *Physics of the Earth and Planetary Interiors*, *25*(4), 297–356. https://doi.org/10.1016/0031-9201(81)90046-7

French, S. W., & Romanowicz, B. (2015). Broad plumes rooted at the base of the Earths mantle beneath major hotspots. *Nature*, *525*(7567), 95–99. https://doi.org/10.1038/nature14876

Garnero, E. J., Grand, S. P., & Helmberger, D. V. (1993). Low *P*-wave velocity at the base of the mantle. *Geophysical Research Letters*, *20*, 1843–1846. https://doi.org/10.1029/93GL02009

Garnero, E. J., & Helmberger, D. V. (1995). A very slow basal layer underlying large-scale low-velocity anomalies in the lower mantle beneath the Pacific: Evidence from core phases. *Physics of the Earth and Planetary Interiors*, *91*, 161–176. https://doi.org/10.1016/0031-9201(95)03039-Y

Garnero, E. J., & Helmberger, D. V. (1996). Seismic detection of a thin laterally varying boundary layer at the base of the mantle beneath the central-Pacific. *Geophysical Research Letters*, *23*, 977–980. https://doi.org/10.1029/95GL03603

Garnero, E. J., McNamara, A. K., & Shim, S.-H. (2016). Continent-sized anomalous zones with low seismic velocity at the base of Earths mantle. *Nature Geoscience*, *9*(7), 481–489. https://doi.org/10.1038/ngeo2733

Grand, S. P. (2002). Mantle shearwave tomography and the fate of subducted slabs. *Philosophical Transactions of the Royal Society of London. Series A: Mathematical Physical and Engineering Sciences*, *360*(1800), 2475–2491. https://doi.org/10.1098/rsta.2002.1077

Havens, E., & Revenaugh, J. (2001). A broadband seismic study of the lowermost mantle beneath Mexico: Constraints on ultralow velocity zone elasticity and density. *Journal of Geophysical Research*, *106*(B12), 30809–30820. https://doi.org/10.1029/2000JB000072

Helmberger, D. V., Wen, L., & Ding, X. (1998). Seismic evidence that the source of the Iceland hotspot lies at the coremantle boundary. *Nature*, *396*(6708), 251–255. https://doi.org/10.1038/24357

Hosseini, K., Sigloch, K., Tsekhmistrenko, M., Zaheri, A., Nissen-Meyer, T., & Igel, H. (2019). Global mantle structure from multifrequency tomography using P PP and P-diffracted waves. *Geophysical Journal International*, *220*(1), 96–141. https://doi.org/10.1093/gji/ggz394

Jackson, M. G., Becker, T. W., & Steinberger, B. (2021). Spatial characteristics of recycled and primordial reservoirs in the deep mantle. *Geochemistry, Geophysics, Geosystems*, *22*(3). https://doi.org/10.1029/2020GC009525

Jackson, M. G., Hart, S. R., Konter, J. G., Kurz, M. D., Blusztajn, J., & Farley, K. A. (2014). Helium and lead isotopes reveal the geochemical geometry of the Samoan plume. *Nature*, *514*(7522), 355–358. https://doi.org/10.1038/nature13794

Jackson, M. G., Hart, S. R., Koppers, A. A. P., Staudigel, H., Konter, J., Blusztajn, J., et al. (2007). The return of subducted continental crust in Samoan lavas. *Nature*, *448*(7154), 684–687. https://doi.org/10.1038/nature06048

Jahnke, G. (2009). *Methods for seismic wave propagation on local and global scales with finite differences*. Ludwig-Maximilians Universtiy.

Jenkins, J., Mousavi, S., Li, Z., & Cottaar, S. (2021). A high-resolution map of Hawaiian ULVZ morphology from ScS phases. *Earth and Planetary Science Letters*, *563*, 116885. https://doi.org/10.1016/j.epsl.2021.116885

Jensen, K. J., Thorne, M. S., & Rost, S. (2013). SPdKS analysis of ultralow-velocity zones beneath the western Pacific. *Geophysical Research Letters*, *40*(17), 4574–4578. https://doi.org/10.1002/grl.50877

Jones, T. D., Davies, D. R., & Sossi, P. A. (2019). Tungsten isotopes in mantle plumes: Heads it's positive, tails it's negative. *Earth and Planetary Science Letters*, *506*, 255–267. https://doi.org/10.1016/j.epsl.2018.11.008

Kim, D., Lekić, V., Ménard, B., Baron, D., & Taghizadeh-Popp, M. (2020). Sequencing seismograms: A panoptic view of scattering in the core-mantle boundary region. *Science*, *368*(6496), 1223–1228. https://doi.org/10.1126/science.aba8972

Kind, R., & Muller, G. (1977). The structure of the outer core from SKS amplitudes and travel times. *Bulletin of the Seismological Society of America*, *67*(6), 1541–1554

Leng, K., Korenaga, J., & Nissen-Meyer, T. (2020). 3-D scattering of elastic waves by small-scale heterogeneities in the Earth's mantle. *Geophysical Journal International*, *223*(1), 502–525. https://doi.org/10.1093/gji/ggaa331

Leng, K., Niseen-Meyer, T., & van Driel, M. (2016). Efficient global wave propagation adapted to 3-D structural complexity: A pseudospectral/spectral-element approach. *Geophysical Journal International*, *207*, 1700–1721. https://doi.org/10.1093/gji/ggw363

Leng, K., Nissen-Meyer, T., van Driel, M., Hosseini, K., & Al-Attar, D. (2019). AxiSEM3D: Broad-band seismic wavefields in 3-D global earth models with undulating discontinuities. *Geophysical Journal International*, *217*(3), 2125–2146. https://doi.org/10.1093/gji/ggz092

Li, M., McNamara, A. K., Garnero, E. J., & Yu, S. (2017). Compositionally-distinct ultra-low velocity zones on Earth's core-mantle boundary. *Nature Communications*, *8*(1). https://doi.org/10.1038/s41467-017-00219-x

McNamara, A. K. (2019). A review of large low shear velocity provinces and ultra low velocity zones. *Tectonophysics*, *760*, 199–220. https://doi.org/10.1016/j.tecto.2018.04.015

Montelli, R., Nolet, G., Dahlen, F. A., & Masters, G. (2006). A catalogue of deep mantle plumes: New results from finite-frequency tomography. *Geochemistry, Geophysics, Geosystems*, *7*(11). https://doi.org/10.1029/2006gc001248

Nelson, P. L., & Grand, S. P. (2018). Lower-mantle plume beneath the Yellowstone hotspot revealed by core waves. *Nature Geoscience*, *11*(4), 280–284. https://doi.org/10.1038/s41561-018-0075-y

Ritsema, J., Deuss, A., van Heijst, H. J., & Woodhouse, J. H. (2010). S40RTS: A degree-40 shear-velocity model for the mantle from new Rayleigh wave dispersion teleseismic traveltime and normal-mode splitting function measurements. *Geophysical Journal International*, *184*(3), 1223–1236. https://doi.org/10.1111/j.1365-246x.2010.04884.x

Rost, S., Garnero, E. J., Williams, Q., & Manga, M. (2005). Seismological constraints on a possible plume root at the core-mantle boundary. *Nature*, *435*, 666–669. https://doi.org/10.1038/nature03620

Rost, S., & Revenaugh, J. (2003). Small-scale ultralow-velocity zone structure imaged by ScP. *Journal of Geophysical Research*, *108*(B1). https://doi.org/10.1029/2001JB001627

Schweitzer, J., & Müller, G. (1986). Anomalous difference traveltimes and amplitude ratios of SKS and SKKS from Tonga-Fiji Events. *Geophysical Research Letters*, *13*(13), 1529–1532. https://doi.org/10.1029/gl013i013p01529

Simmons, N. A., Myers, S. C., Johannesson, G., & Matzel, E. (2012). LLNL-G3Dv3: Global P wave tomography model for improved regional and teleseismic travel time prediction. *Journal of Geophysical Research*, *117*, B10302. https://doi.org/10.1029/2012JB009525

Spica, Z., Perton, M., & Beroza, G. C. (2017). Lateral heterogeneity imaged by small-aperture ScS retrieval from the ambient seismic field. *Geophysical Research Letters*, *44*, 8276–8284. https://doi.org/10.1002/2017GL073230

Thorne, M. S., Garnero, E. J., Jahnke, G., Igel, H., & McNamara, A. K. (2013). Mega ultra low velocity zone and mantle flow. *Earth and Planetary Science Letters*, *364*, 59–67. https://doi.org/10.1016/j.epsl.2012.12.034

Thorne, M. S., Leng, K., Pachhai, S., Rost, S., Wicks, J., & Nissen-Meyer, T. (2021). The most parsimonious ultralow-velocity zone distribution from highly anomalous SPdKS waveforms. *Geochemistry, Geophysics, Geosystems*, *22*(1). https://doi.org/10.1029/2020gc009467

Thorne, M. S., Pachhai, S., Leng, K., Wicks, J. K., & Nissen-Meyer, T. (2020). New candidate ultralow-velocity zone locations from highly anomalous SPdKS waveforms. *Minerals*, *10*(3), 211. https://doi.org/10.3390/min10030211

Thorne, M. S., Takeuchi, N., & Shiomi, K. (2019). Melting at the edge of a slab in the deepest mantle. *Geophysical Research Letters*, *46*(14), 8000–8008. https://doi.org/10.1029/2019gl082493

Thorne, M. S., Zhang, Y., & Ritsema, J. (2013). Evaluation of 1-D and 3-D seismic models of the Pacific lower mantle with S SKS and SKKS traveltimes and amplitudes. *Journal of Geophysical Research: Solid Earth*, *118*(3), 985–995. https://doi.org/10.1002/jgrb.50054

Waszek, L., Thomas, C., & Deuss, A. (2015). PKP precursors: Implications for global scatterers. *Geophysical Research Letters*, *42*, 3829–3838. https://doi.org/10.1002/2015GL063869

Wen, L. (2000). Intense seismic scattering near the Earths core-mantle boundary beneath the Comoros hotspot. *Geophysical Research Letters*, *27*(22), 3627–3630. https://doi.org/10.1029/2000gl011831

Wen, L., & Helmberger, D. V. (1998a). A two-dimensional P-SV hybrid method and its application to modeling localized structures near the core-mantle boundary. *Journal of Geophysical Research*, *103*, 17901–17918. https://doi.org/10.1029/98JB01276

Wen, L., & Helmberger, D. V. (1998b). Ultra-low velocity zones near the core-mantle boundary from broadband PKP precursors. *Science*, *279*, 1701–1703. https://doi.org/10.1126/science.279.5357.1701

Wessel, P., & Smith, W. H. F. (1998). New improved version of generic mapping tools released. *Eos, Transactions, American Geophysical Union*, *79*(47), 579. https://doi.org/10.1029/98eo00426

Wicks, J. K., Jackson, J. M., & Sturhahn, W. (2010). Very low sound velocities in iron-rich (Mg,Fe)O: Implications for the core-mantle boundary region. *Geophysical Research Letters*, *37*(15). https://doi.org/10.1029/2010gl043689

Williams, Q., & Garnero, E. J. (1996). Seismic evidence for partial melt at the base of Earth's mantle. *Science*, *273*(5281), 1528–1530. https://doi.org/10.1126/science.273.5281.1528

Williams, Q., Revenaugh, J., & Garnero, E. (1998). A correlation between ultra-low basal velocities in the mantle and hot spots. *Science*, *281*(5376), 546–549. https://doi.org/10.1126/science.281.5376.546

Yuan, K., & Romanowicz, B. (2017). Seismic evidence for partial melting at the root of major hot spot plumes. *Science*, *357*(6349), 393–397. https://doi.org/10.1126/science.aan0760

Zhang, J., Lv, J., Li, H., Feng, X., Lu, C., Redfern, S. A. T., et al. (2018). Rare helium-bearing compound FeO_2He stabilized at deep-earth conditions. *Physical Review Letters*, *121*. https://doi.org/10.1103/PhysRevLett.121.255703

Zhang, Y., Ritsema, J., & Thorne, M. S. (2009). Modeling the ratios of SKKS and SKS amplitudes with ultra-low velocity zones at the core-mantle boundary. *Geophysical Research Letters*, *36*(19). https://doi.org/10.1029/2009gl040030

Zhao, C., Garnero, E. J., Li, M., McNamara, A., & Yu, S. (2016). Intermittent and lateral varying ULVZ structure at the northeastern margin of the Pacific LLSVP. *Journal of Geophysical Research: Solid Earth*, *122*, 1198–1220. https://doi.org/10.1002/2016JB013449